electronics

MDPI

Article

Control Design of Observer-Based Virtual Soft Boundary for a Power-Assist System with Limited Operating Range

Po-Wen Hsueh *, Wu-Sung Yao and Tien-Min Kao

Department of Mechatronics Engineering, National Kaohsiung University of Science and Technology, No.1 University Rd., Yanchao District, Kaohsiung City 824, Taiwan; wsyao@nkust.edu.tw (W.-S.Y.); tnnkao@gmail.com (T.-M.K.)

* Correspondence: hpowen@nkust.edu.tw; Tel.: +886-7-6011000 (ext. 32212)

Abstract: Control design of power-assist systems has been widely applied to human-robot interactive systems such as wearable exoskeleton systems, of which the range of motion limitation of human joints in the power-assist systems is essential. This paper presents a virtual soft boundary design for a human-robot cooperation system with a limited operating range. The proposed virtual soft boundary is realized by impedance control and integrated into the power-assist robot arm system; meanwhile, power-assist robot arm systems are typical human-in-the-loop systems, and the control of the power-assist system in performing in accordance with a human's perception is a significant issue. Therefore, a model-based disturbance observer with a pseudo-derivative feedback feedforward (PDFF) compensator is designed to effectively estimate the human's torque for an appropriate motor torque command. Experimental results show that the proposed control method can estimate the human torque exerted on the robot arm system to achieve a power-assist system, and the virtual soft boundary can be realized by the impedance control and integrated into the power-assist robot arm system.

Keywords: disturbance estimation; PDFF controller; power-assist system; virtual soft boundary; impedance control

Citation: Hsueh, P.-W.; Yao, W.-S.; Kao, T.-M. Control Design of Observer-Based Virtual Soft Boundary for a Power-Assist System with Limited Operating Range. *Electronics* **2022**, *11*, 690. https://doi.org/10.3390/electronics11050690

Academic Editors: Maysam Abbod and Boris Andrievsky

Received: 12 January 2022
Accepted: 19 February 2022
Published: 23 February 2022

1. Introduction

The concept of a power-assist system, which was first discussed by the Cornell Aeronautical Laboratory in 1968 [1], was a concept with the purpose of assisting people with disabilities by using a wearable exoskeleton. The evolution of robotics research over the last 50 years has also pointed out the significance of power-assist technology developed in robotics research [2]. Hence, the control design of power-assist techniques is indeed essential for the human-robot interactive system. Moreover, service robots incorporating physical human-robot interaction (pHRI) have recently become an important trend outside industrial applications for addressing the new needs and markets in daily human life [3–6]. The general ability of service robots makes it necessary to work closely with humans; thus, researching control techniques for pHRI should be central in the development of service robots [7]. Control design of power-assist devices is regarded as an essential technique for dealing with pHRI because of its compliance design, and it has recently been investigated in several service robots, such as power-assisted wheelchairs [5], cycle ergometers for stroke rehabilitation [8], walking assisted robots [9], ankle rehabilitation robotic devices [10], and so on.

Control design of a power-assist system can be defined as assistance to motions for the purpose of enhancing user mobility or reducing user effort. Power assistance supported by servo motors is not intended to entirely replace user effort. The power-assist system is operated in accordance with a user's perception; hence, the servo motor should be sensitive to the force the user exerts on the system [11,12]. Force sensors are a

straightforward solution for obtaining user force information. However, directly detecting user force by sensors is not practical for implementation due to the problems of installation and wiring. To overcome the sensing issue, several studies on sensing indirect force have been developed, such as a strain gauge device equipped with a Wheatstone bridge, which has been integrated into a robotic rehabilitation exoskeleton for a user's tremor force assessment [13]. Additionally, an angle sensor, a linear potentiometer, and touch sensors were designed to monitor the torque of the user's below-knee exoskeleton [14]. Furthermore, a load cell collocated with a linear encoder has been employed to develop a torque-controllable actuator for the knee assistance device [15]. However, the structure of those indirect sensing devices still involves issues of installation and wiring.

Therefore, using model-based observers instead of force sensors has been recommended for estimating the human propel efforts of power-assist systems [5,6,8,16], in which only the excitation signal (i.e., the current input of a servo motor) and a measurable feedback signal (i.e., the motor position output information) are necessary for the presented observer. Further, the structure of the model-based observer primarily consists of five elements: excitation signal of the control system, sensor output, mathematical model of the control plant, a mathematical model of the sensor, and an observer compensator. Although the performance of an observer compensator with a pseudo-derivative feedback (PDF) controller has been verified in [6,8,16], the pseudo-derivative feedback feedforward (PDFF) controller is proposed to improve the transient response of the estimated external force in this study.

Moreover, various power assist human-robot systems, especially in wearable exoskeletons, are performed in accordance with the user's joint motion. Therefore, it is essential to achieve the compliance characteristics in the power-assist system [17]. For example, an admittance control of powered exoskeletons based on joint torque estimation was presented to render a trajectory-free compliance control law [18]; then, to ensure recursive feasibility and constraint compliance, the predictive control of a tube-based model was employed to regulate a knee joint with functional electrical stimulation [19]. Further, the full-active electro-hydrostatic powered ankle prosthesis was implemented to provide initiative compliance while assisting push-off at the end of the stance phase [20]. However, the range of motion (*ROM*) of human joints is generally operated with limitations while the joint is flexing or extending. The demand of the virtual soft boundary must be realized in the power-assist human-robot systems to avoid the risk of extreme flexing or extending. Hence, the virtual soft boundary realized by the impedance control is integrated with the disturbance estimation to achieve the compliant operation of the power assist human-robot system, constrained by the *ROM* of the human joints.

The remainder of this paper is organized as follows: Section 2 discusses the dynamics model of a one-link robot arm and the design of the model-based disturbance observer. Then, the range planning of *ROM*, control design of the power-assisted mode, and impedance control are proposed to deal with the limited operating range in Section 3. Further, the experiment results and discussion are presented in Section 4. A conclusion is then provided in Section 5.

2. Dynamics Modeling and Disturbance Estimation

2.1. System Dynamic Modeling

In order to validate the assistant control approach, this study applied the proposed control system to a one-link robot arm driven by an electric motor. The demonstration set-up with a single degree-of-freedom is illustrated in Figure 1, where the end of the robot arm can be forced by human force. Then, an electric motor can be used to amplify the operator's force for the driven loading. Further, the dynamic model of the controlled system was conducted to investigate the power-assist system driven by the human force.

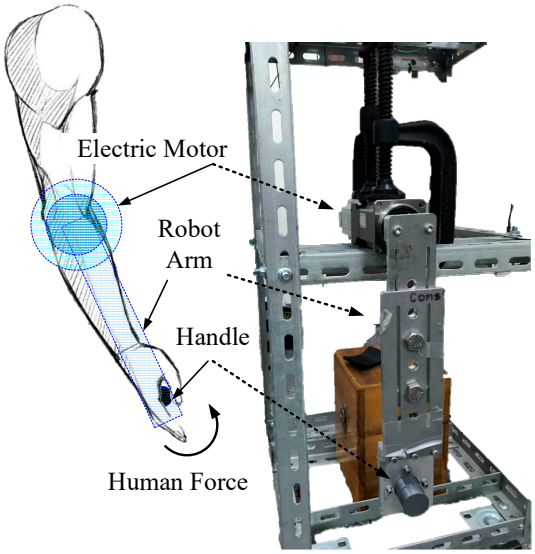

Figure 1. Experimental setup of the power-assist system.

Based on Figure 1, Figure 2 shows a schematic view of the one-link robot arm model, where C presents the mass center of the robot arm, L denotes the length of the original point O to the handle of the robot arm, and L_c indicates the length of $\overline{OC}$. Additionally, θ_{arm} presents the angular position of the robot arm. Then, the total kinetic and potential energy function can be employed to derive the dynamic equations of the system in Figure 2. Here, the kinetic and potential energy function is considered by the Lagrangian function L given by

$$L = \frac{1}{2} M_c {v_c}^2 + \frac{1}{2} I_c \dot{\theta}_{arm}^2 + M_c L_c g \cos(\theta_{arm}) \tag{1}$$

where M_c denotes the total mass of the one-link robot arm, $v_c (= L_c \dot{\theta}_{arm})$ indicates the tangent velocity of the center of mass of the robot arm, and I_c represents the inertia of the one-link robot arm with respect to the vertical axis through C.

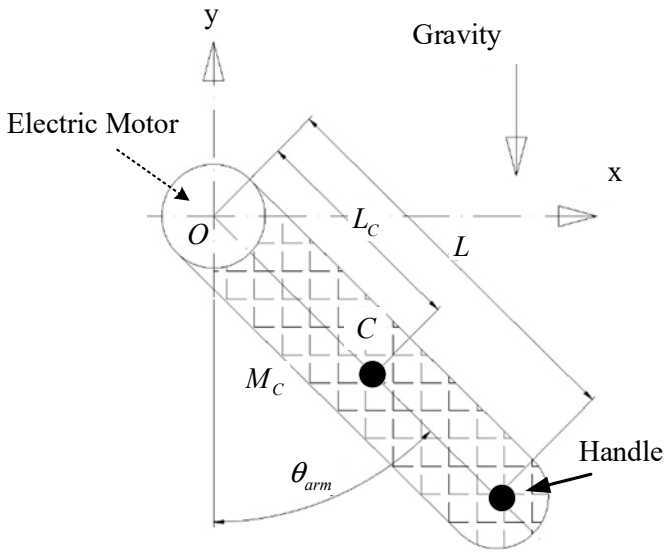

Figure 2. Schematic representation of the one-link robot arm.

Furthermore, to include the dissipated energy caused by viscous friction, the additional term of the dissipation function $D = B_e \dot{\theta}_{arm}^2 / 2$ is obtained, where B_e presents the equivalent

viscous coefficient of the system. Thus, the dynamic equation of the one-link robot arm is governed by:

$$\frac{d}{dt}\left(\frac{\partial L}{\partial \dot{\theta}_{arm}}\right) - \frac{\partial L}{\partial \theta_{arm}} + \frac{\partial D}{\partial \dot{\theta}_{arm}} = \tau_m \tag{2}$$

where τ_m indicates the electric motor torque output. Let $\tau_m = k_t n i_a$, where k_t is the torque constant of the driving motor, n is the gear reduction ratio, and i_a denotes the input current of the driving motor. Solving the Lagrange equation will yield the dynamics model of the one-link robot arm:

$$\tau_m = J_e\ddot{\theta} + B_e\dot{\theta} + M_c L_c g \sin(\theta_{arm}) \tag{3}$$

where $J_e(= M_c L_c^2 + I_c)$ is the equivalent inertia of the one-link robot arm. Then, the block diagram of the one-link robot arm model is described in Figure 3. In order to obtain the parameter of the system in Figure 3, the mathematical model is calculated by spectrum analysis of the frequency response of the proposed system. Therefore, the parameters of J_e = 0.2379 kg·m^2 and B_e = 0.5545 Nm/(rad/s) can be obtained. Additionally, the friction model recognized by [21] is depicted in Figure 4. The static and Coulomb friction is described in Table 1 and applied to compensate for the friction in the control system.

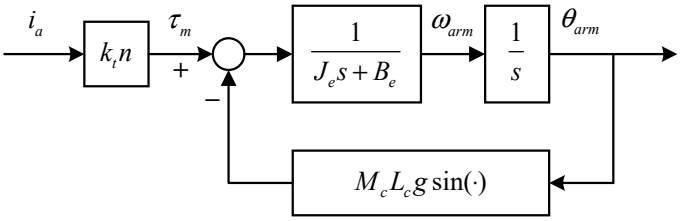

Figure 3. Block diagram of the one-link robot arm model.

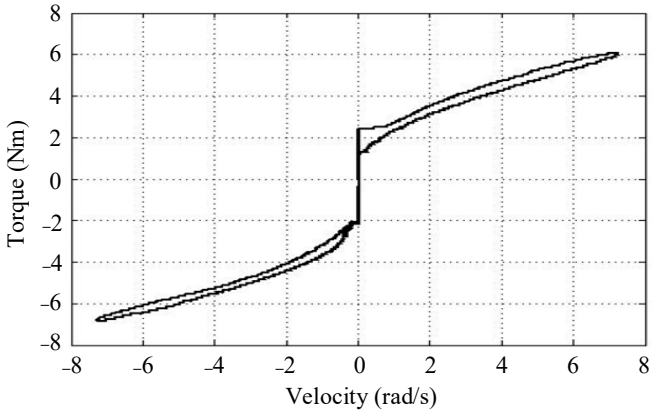

Figure 4. Friction model of the one-link robot arm.

Table 1. Parameter of the friction model.

	Static Friction (Nm)	Viscous Coefficient (Nm/(rad/sec))
Clockwise	2.189	0.60
Counter clockwise	3.026	0.59

2.2. External Disturbance Estimation

According to previous analyses, the one-link robot arm system can be modeled as in Figure 3, where J_e and B_e indicate the equivalent inertia and viscous coefficient of the system. Then, k_t and i_a are the torque constant and current input of an electric motor. Further, ω_{arm} and θ_{arm} present the angular velocity and position information of the robot arm. Suppose that T_{dis} denotes the external disturbance of the system, which consists of

the external human propel torque T_h, the friction T_f, and the gravity effect T_g. Thus, T_{dis} can be expressed as:

$$T_{dis} = T_h + T_f + T_g \tag{4}$$

where $T_g = M_c L_c g \sin(\theta_{arm})$. Since the parameter of the friction model T_f can be obtained from Figure 4 and Table 1, the input of the propelled external human torque in the system can be given by:

$$T_h = T_{dis} - T_g - T_f \tag{5}$$

Hence, the human propelled input can be estimated by T_{dis}. In this study, the model-based observer applied for estimating the human's propel effort was developed by [22]. In general, the model-based observer primarily consists of five elements: plant excitation signal, real sensor output, an estimated model of the control plant, a model of the sensor, and an observer compensator. Assume that the angular velocity of the robot arm system can be measured. Then, the one-link robot arm system combined with the model-based observer can be presented as in Figure 5, where i_a indicates the system excitation signal, ω_{arm} is the real sensor output, $1/(\hat{J}_e s + \hat{B}_e)$ presents the estimated model of the control plant, and $G_{co}(s)$ denotes the observer compensator. Moreover, the model of the sensor is assumed to be equal to one. Since converging the observed error, $E = \omega_{arm} - \hat{\omega}_{arm}$ is one of the primary issues in the model-based observer and properly designing the observer compensator $G_{co}(s)$ is essential.

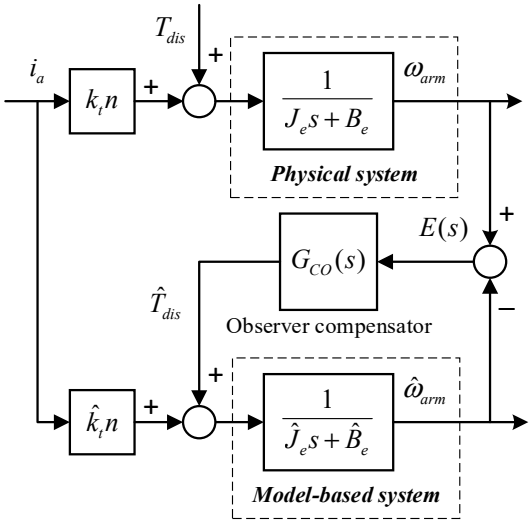

Figure 5. Model-based observer utilized in the one-link robot arm system.

From Figure 5, an appropriate design of the compensator $G_{co}(s)$ is similar to regulating a compensator in a speed feedback control system, which can be found in Figure 6. Although the performance of the compensator $G_{co}(s)$ designed by a PDF controller [6,8,23] has been verified, a PDFF controller is proposed to improve the transient response of the external disturbance estimation in this study. The observer compensator formed by the PDFF controller is illustrated in Figure 7, where K_p and K_i are the proportional and integral gain of the observer compensator, respectively. Furthermore, K_{ff} is an additional feedforward gain. It can be seen that the PDFF controller constitutes a generalized PDF controller $K_{ff} = 0$. Suppose that $G_v(s)$ is the transfer function from ω_{arm} to $\hat{\omega}_{arm}$. Thus, we have

$$\frac{\hat{\omega}_{arm}}{\omega_{arm}} = G_v(s) = \frac{K_{ff} K_p s + K_i K_p}{\hat{J}_e s^2 + (K_p + \hat{B}_e) s + K_i K_p} \tag{6}$$

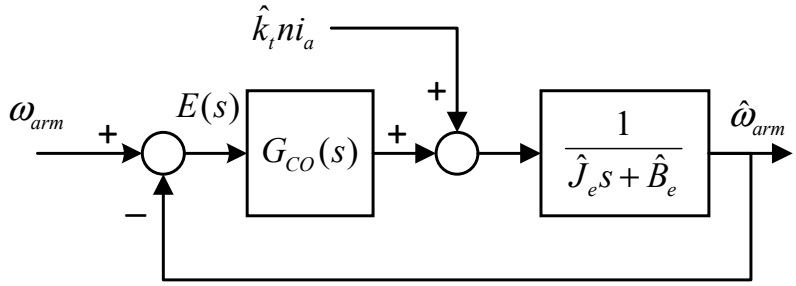

Figure 6. Observer utilized in the one-link robot arm system.

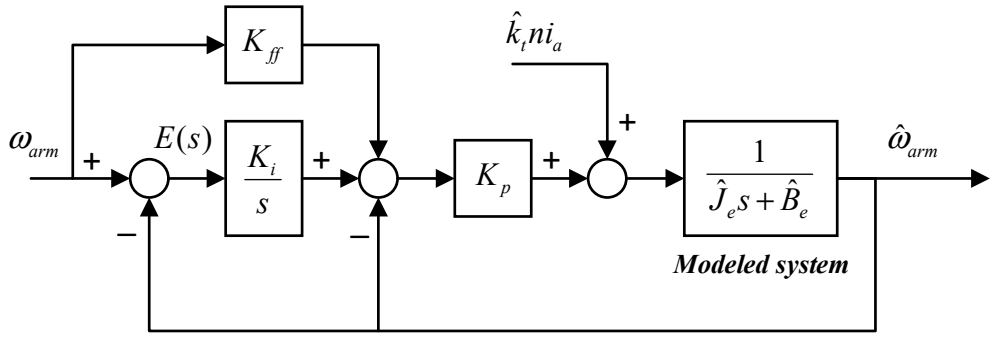

Figure 7. Observer compensator formed by the PDFF controller.

To compare the PDF controller in [8] and the PDFF controllers in Figure 7, (6) can be represented by a second-order low-pass filter with the desired natural frequency ω_{nOB} and damping ratio ς_{OB}, such as:

$$G_v(s) = \frac{K_{ff}K_p s/\hat{J}_e + K_i K_p/\hat{J}_e}{s^2 + (\hat{B}_e + K_p)s/\hat{J}_e + K_i K_p/\hat{J}_e} = \frac{K_{ff}(2\zeta_{OB}\omega_{nOB} - \hat{B}_e/\hat{J}_e)s + {\omega_{nOB}}^2}{s^2 + 2\zeta_{OB}\omega_{nOB}s + {\omega_{nOB}}^2} \quad (7)$$

where

$$\begin{cases} {\omega_{nOB}}^2 = K_i K_p/\hat{J}_e \\ 2\zeta_{OB}\omega_{nOB} = (\hat{B}_e + K_p)/\hat{J}_e \end{cases} \text{ and } \begin{cases} K_p = 2\zeta_{OB}\omega_{nOB}\hat{J}_e - \hat{B}_e \\ K_i = {\omega_{nOB}}^2 \hat{J}_e/K_p \end{cases} \quad (8)$$

From (7) and according to the definition of bandwidth in the second-order system, we have:

$$\left| \frac{K_{ff}(2\zeta_{OB}\omega_{nOB} - \hat{B}_e/\hat{J}_e)(j\omega_{bwOB}) + \omega_{nOB}^2}{(j\omega_{bwOB})^2 + 2\zeta_{OB}\omega_{nOB}(j\omega_{bwOB}) + \omega_{nOB}^2} \right| = \frac{1}{\sqrt{2}} \quad (9)$$

Assume that $\hat{B}_e$ can be initially compensated; thus the natural frequency ω_{nOB} in the observer is obtained by the relationship of (9) [24].

Suppose that the low-speed movement of the human robot-arm system is chosen to avoid damage. The bandwidth and damping ratio in the second-order system of (7) is designed by ω_{bwOB} = 30 rad/s (≈4.77 Hz) and ζ_{OB}=1 (critically damped). Therefore, the designed parameters of the observer are listed in Table 2. Further, the performance of the step response in the observer design is depicted in Figure 8, where the solid line presents the result of the observer while K_{ff} = 0, and the dash-dotted line indicates the performance of the observer with the feedforward gain tuned by K_{ff} = 0.25. Since the PDFF controller is equivalent to a generalized PDF controller of K_{ff} = 0, the transient response of PDFF 25 is better than that of the PDF (PDFF 0). Further, the rising time is improved from 0.072 s. (PDFF0) to 0.053 s. (PDFF25). Hence, in this study, the PDFF controller K_{ff} = 0.25 is integrated into the model-based observer design for estimating external disturbance.

Table 2. Parameters and transient response of the observer compensator.

	PDFF0 (PDF)	**PDFF25**
Bandwidth (rad/sec)	ω_{bwOB} = 30	ω_{bwOB} = 30
Damping Ratio	ζ_{OB} = 1	ζ_{OB} = 1
Nature Frequency (rad/sec)	ω_{nOB} = 46.61	ω_{nOB} = 141.42
Observer Parameter	$\begin{cases} K_i = 465.16 \\ K_p = 19.96 \\ K_{ff} = 0 \end{cases}$	$\begin{cases} K_i = 282.84 \\ K_p = 70.71 \\ K_{ff} = 0.25 \end{cases}$

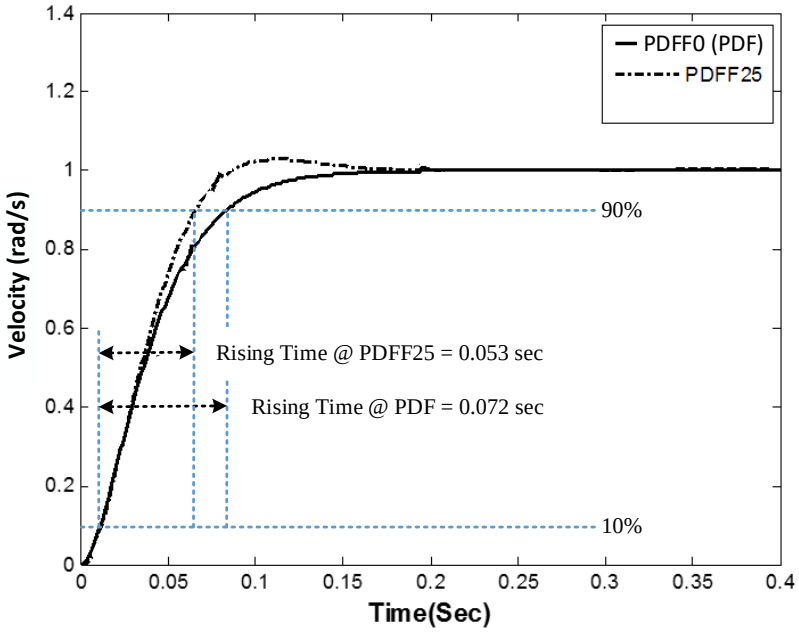

Figure 8. The step response of the observer design.

However, the actual sensor output of the one-link robot arm system is θ_{arm} (measured by the incremental optical encoder). Further, the PDFF controller can be implemented as in Figure 9a. To use the measured position information for speed control and torque observer design, the structure of Figure 9a can be redrawn by the equivalent block diagram illustrated in Figure 9b. Considering practical implementation, the proposed disturbance observer integrated with the structure of Figure 9b is shown in Figure 10, in which only the measured motor current (input) i_a and position (output) θ_{arm} are utilized to estimate the external disturbance T_{dis}. From Figure 10, the transfer function between actual disturbance input T_{dis} and estimated disturbance $\hat{T}_{dis}$ is given by:

$$\frac{\hat{T}_{dis}}{T_{dis}} = \frac{\left(\hat{J}_e s + \hat{B}_e\right)}{\left(J_e s + B_e\right)} \cdot \frac{K_{ff}K_p s/\hat{J}_e + K_i K_p/\hat{J}_e}{s^2 + \left(\hat{B}_e + K_p\right)/\hat{J}_e s + K_i K_p/\hat{J}_e} = \frac{\left(\hat{J}_e s + \hat{B}_e\right)}{\left(J_e s + B_e\right)} G_v(s) \tag{10}$$

Assuming that the estimated equivalent inertia $\hat{J}_e$ and viscous coefficient $\hat{B}_e$ of the one-link robot arm is approximated to the actual equivalent inertia J_e and viscous coefficient B_e, (10) can therefore be rewritten as:

$$\frac{\hat{T}_{dis}}{T_{dis}} \approx \frac{K_{ff}K_p s/\hat{J}_e + K_i K_p/\hat{J}_e}{s^2 + \left(\hat{B}_e + K_p\right)/\hat{J}_e s + K_i K_p/\hat{J}_e} = G_v(s) \tag{11}$$

where the performance of $G_v(s)$ can be analyzed by (7)–(9) in the previous description. In other words, this indicates that the human propel effort T_h can be obtained based on the proposed observer as:

$$\hat{T}_h = \hat{T}_{dis} - \hat{T}_g - \hat{T}_f \tag{12}$$

where the performance of the estimated $\hat{T}_h$ can be conducted in the following experimental section.

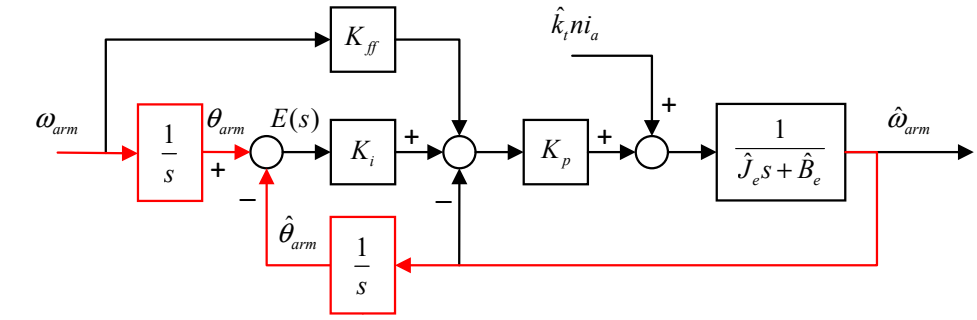

(**a**) Block diagram modified from Figure 7

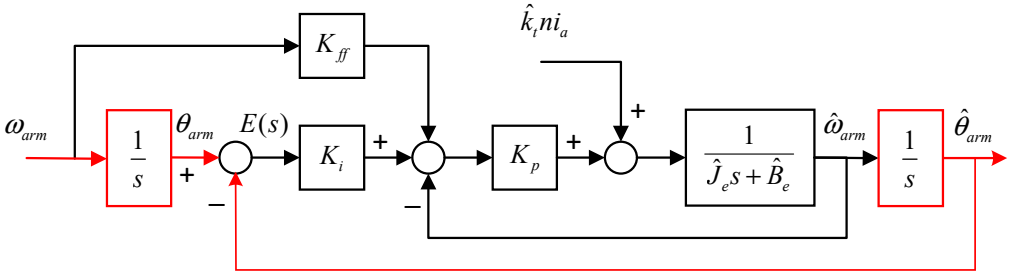

(**b**) Observer constructed from Figure 9a

Figure 9. The modification of the observer design.

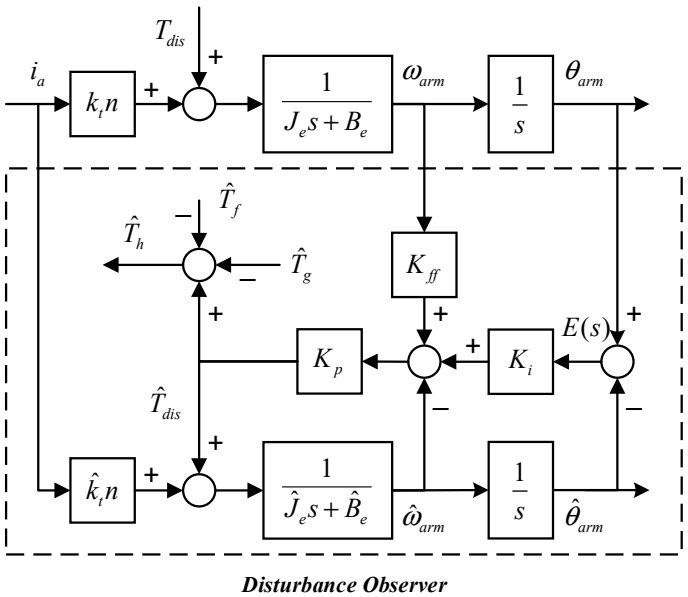

Figure 10. Proposed disturbance observer.

3. Control Design of Power-Assist System with Limited Operating Range

In general, the range of motion (*ROM*) of human joints is operated with limitations while the joint is flexing or extending. Hence, it is necessary to consider the issue of limited operation in a power-assist system. Figure 11 presents the control strategy of a power-assist system with an operating limitation in the one-link robot arm system, where θ_{ROM} indicates

the *ROM*, θ_{IMP} shows the angle range of the impedance mode, and θ_{PAC} presents the angle range of the power-assisted control mode. According to the control strategy in Figure 11, the torque sensorless power-assist system integrated by the impedance control is proposed in Figure 12, where the robot arm system is mentioned in the previous section. Further, T_{sys} is the power-assisted control law and can be designed as

$$T_{sys} = \begin{cases} T_{imp}, \text{ for } 0 \le \theta_{arm} < \theta_{IMP} \text{ or } (\theta_{IMP} + \theta_{PAC}) \le \theta_{arm} < \theta_{ROM} \\ T_{pac}, \text{ for } \theta_{IMP} \le \theta_{arm} < (\theta_{IMP} + \theta_{PAC}) \end{cases} \tag{13}$$

where T_{imp} is the power-assisted command of the impedance mode in the intervals of A and C. Then, $T_{pac} = A_T \hat{T}_h$ indicates the command of the power-assisted mode in the interval of B with the power-assisted ratio A_T.

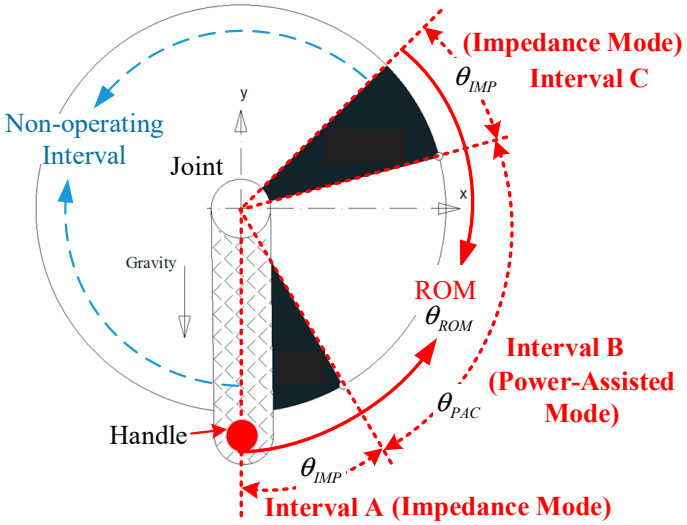

Figure 11. Control strategy of power-assist system with operating limitation.

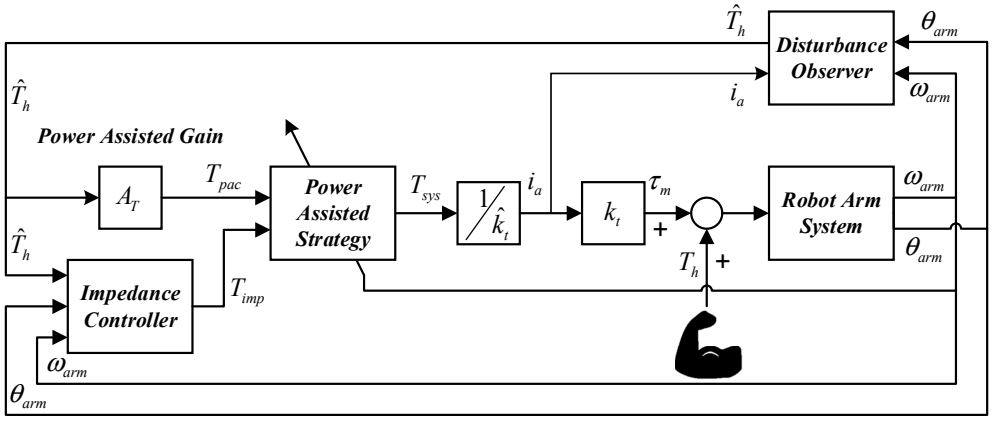

Figure 12. Control structure of the torque sensorless power-assist system with impedance controller.

In the intervals of A and C, impedance control is applied to improve the safety of human-robot interaction in the boundary of *ROM* [25]. Thus, the impedance control scheme can be designed as Figure 13, where the inner-loop is the velocity loop control with the adjustable parameters k_{imp1} and k_{imp2}. The outer-loop dominates the position feedback control with a proportional gain k_{imp3}. Furthermore, the θ^*_{arm} is the desired position command generated by the required impedance model of the inertia J_{imp}, damping B_{imp}, and stiffness K_{imp}.

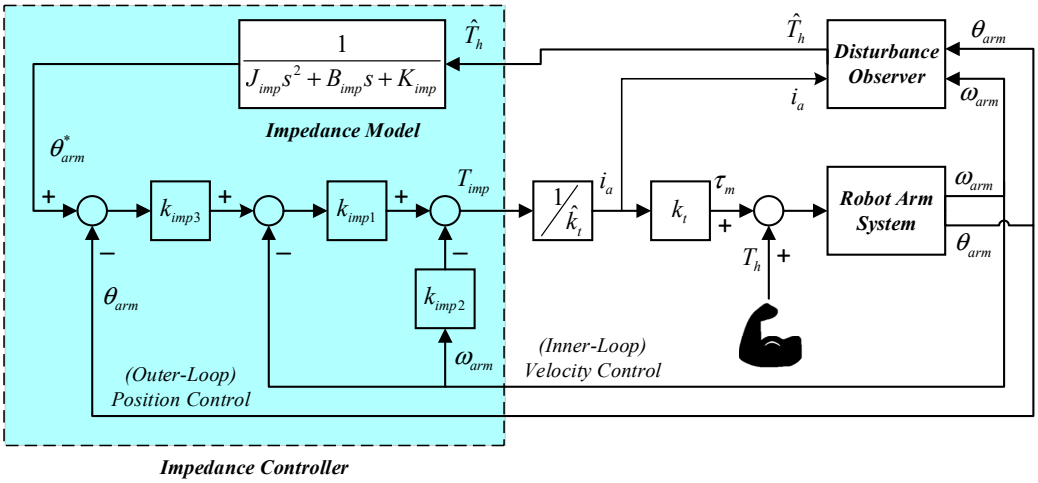

Figure 13. Structure of the proposed impedance controller.

Moreover, due to the fact that Interval B presents the power-assisted mode, the power-assisted control law T_{sys} in Interval B can be designed as:

$$T_{sys} = T_{pac} = A_T \hat{T}_h \tag{14}$$

where A_T is represented as the power-assisted ratio and $\hat{T}_h$ indicates the estimated human propel input. To verify the stability of the power-assisted mode, the block diagram of the power-assisted mode is illustrated in Figure 14. Thus, the estimated human input $\hat{T}_h$ can be expressed by

$$\hat{T}_h = K_p\left(K_{ff}\omega_{arm} + K_i E(s) - \hat{\omega}_{arm}\right) \tag{15}$$

where $E(s) = \theta_{arm} - \hat{\theta}_{arm} = (\omega_{arm} - \hat{\omega}_{arm})/s$. Assuming that the estimated equivalent inertia $\hat{J}_e$, viscous coefficient $\hat{B}_e$, and motor torque constant $\hat{k}_t$ of the one-link robot arm are approximated to the actual equivalent inertia J_e, viscous coefficient B_e and motor torque constant k_t, (15) can therefore be rewritten as:

$$\hat{T}_h = \frac{K_p K_{ff} s + K_p K_i}{\hat{J}_e s^2 + (\hat{B}_e + K_p)s + K_p K_i} T_h + \frac{(K_{ff} - 1)K_p s}{\hat{J}_e s^2 + (\hat{B}_e + K_p)s + K_p K_i} T_{pac} \tag{16}$$

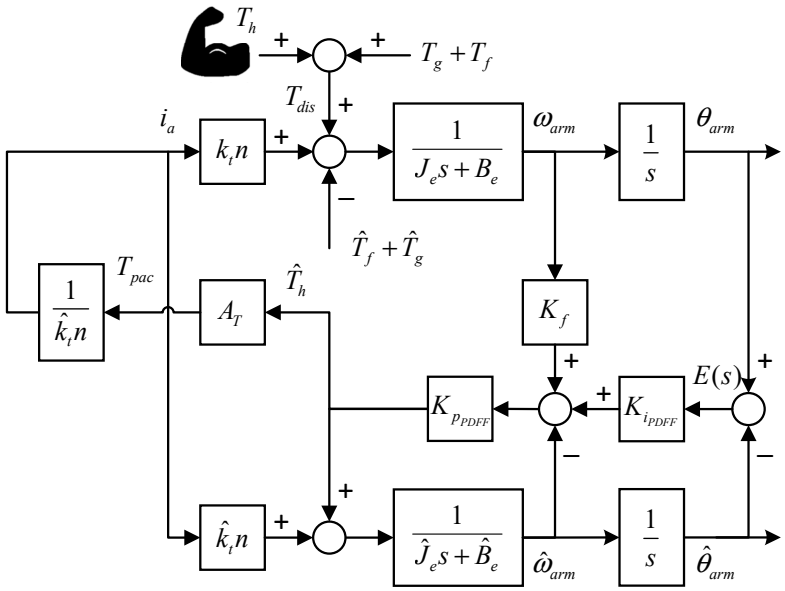

Figure 14. Block diagram of the control design of power-assisted mode.

According to (14) and (16), the transfer function of the estimated human input $\hat{T}_h$ in the power-assisted control mode is conducted by:

$$\frac{\hat{T}_h}{T_h} = \frac{K_{P_{PDFF}} K_f s + K_{P_{PDFF}} K_{i_{PDFF}}}{\hat{J}_e s^2 + \left[\hat{B}_e + K_{P_{PDFF}} + (K_{P_{PDFF}} - K_f) A_T\right] s + K_{P_{PDFF}} K_{i_{PDFF}}} \tag{17}$$

Meanwhile, the root locus and frequency response of (17) are shown in Figures 15 and 16, respectively. Obviously, the system is stable with the design of the power-assisted ratio A_T = 0 ~ 10.

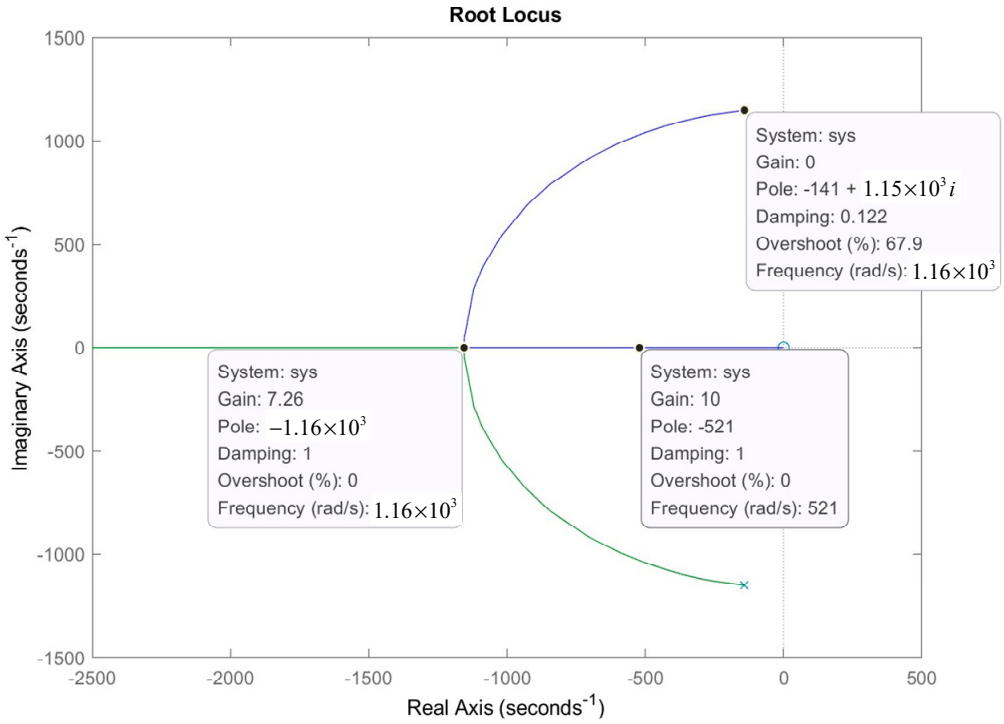

Figure 15. Root locus of the power-assisted mode with A_T.

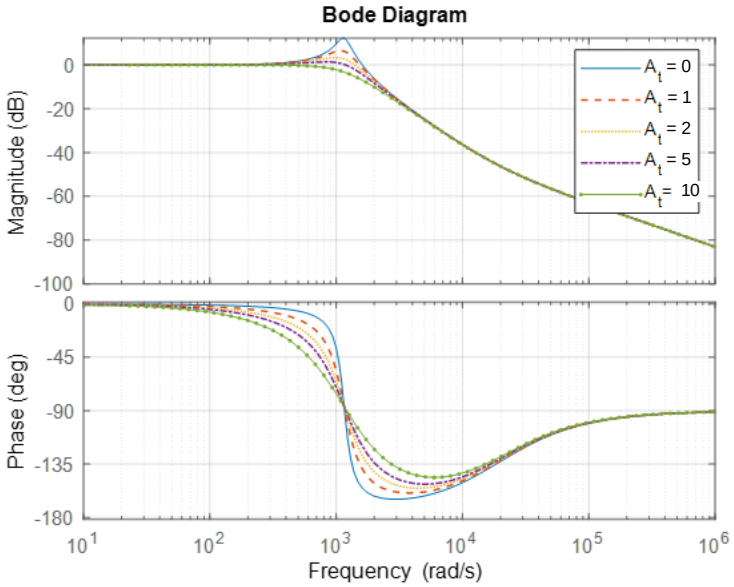

Figure 16. Bode plot of power-assisted mode with A_T.

4. Experimental Verification

4.1. Experimental System

Figure 17 presents an experimental system of this study, where a DSP-based controller is an intelligent motion control platform with a PowerPC 400 embedded processor. The one-link robot arm is driven by a 400 W electric motor with the resolution 2500 pulses/rev of the encoder and a gear ratio $n = 40$ of the gearbox. Further, the ADXL335 accelerometer is utilized to measure the position θ_{arm} of the robot arm. The parameters of the robot arm in Figure 3 are obtained by spectrum analysis of the frequency response of the proposed system, where $\hat{k}_t = 1.3/3$ Nm/A, $\hat{J}_e = 0.2379$ kg·m^2, and $\hat{B}_e = 0.5545$ Nm/(rad/s).

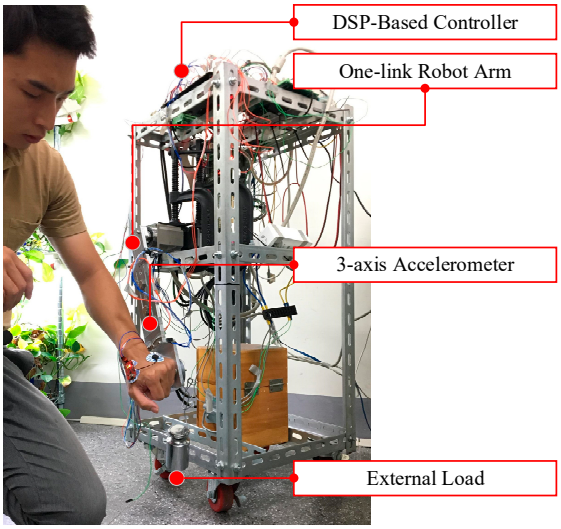

Figure 17. Experimental setup of the one-link robot arm.

4.2. Verification of Disturbance Estimating

The effectiveness of the proposed disturbance observer is confirmed by experiments with a load weight m_{load} on the end of the robot arm. Thus, the load torque T_{load} can be obtained by:

$$T_{load} = m_{load} g L \sin(\theta_{arm}) \tag{18}$$

Then, the experimental progress is that the robot arm makes a circular motion with a fixed angular velocity ω_{arm} as shown in Figure 18. Further, the estimated load torque of the experimental results is similar to (12) and can be described by:

$$\hat{T}_{load} = \hat{T}_{dis} - \hat{T}_g - \hat{T}_f \tag{19}$$

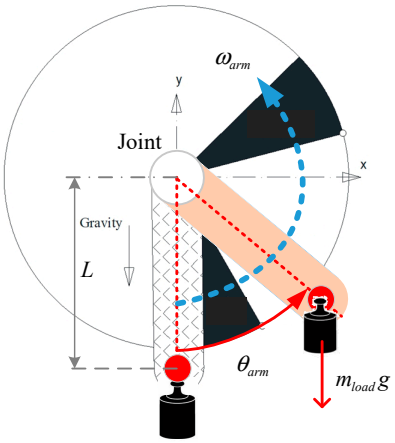

Figure 18. Testing loads at the end of the robot arm.

Subsequently, theoretical and experimental results were compared to examine validity. The load torque following the three cases at ω_{arm}^{ref} = 10 RPM with the proposed disturbance observer was conducted by three cases, i.e., case A: m_{load} = 0 kg, case B: m_{load} = 0.5 kg, and case C: m_{load} = 1 kg. Figure 19 shows the velocity control structure utilized to verify the disturbance estimation, where the transfer function from ω_{arm}^{ref} to ω_{arm} is formulated as:

$$\frac{\omega_{arm}}{\omega_{arm}^{ref}} = \frac{k_{iv}\hat{k}_t n/\hat{J}_e}{s^2 + (\hat{B}_e + k_{pv}\hat{k}_t n)s/\hat{J}_e + k_{iv}\hat{k}_t n/\hat{J}_e} = \frac{{\omega_n}^2}{s^2 + 2\zeta\omega_n s + {\omega_n}^2} \tag{20}$$

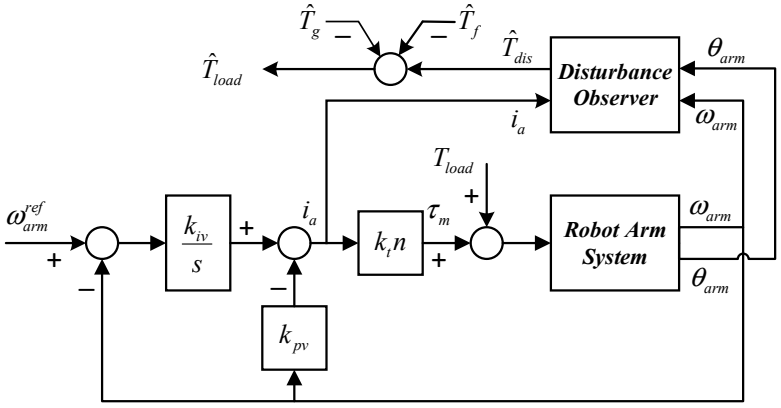

Figure 19. Velocity control structure for verifying the disturbance observer.

It can be seen from (20), that the controller parameters are related to a standard second-order system. Choosing the natural frequency $\omega_n = 2\pi \times 10$ rad/s and the damping ratio ζ = 1, the integral and proportional gains k_{iv} and k_{pv}, respectively, of the velocity control are given by:

$$\begin{cases} k_{iv} = ({\omega_n}^2 \hat{J}_e)/(\hat{k}_t n) = 54.18 \\ k_{pv} = (2\zeta\omega_n \hat{J}_e - \hat{B}_e)/(\hat{k}_t n) = 1.69 \end{cases} \tag{21}$$

Experimental results corresponding to the three cases are presented in Figures 20–22. First, the velocity response is anticipated to be 10 RPM with insignificant variation in each condition. From (19), the estimated load torque should be equal to zero while m_{load} = 0 kg of case A. Thus, the dashed line presents the theoretical value shown in Figure 20c, whereas the dotted line is the load torque estimated by the proposed disturbance observer in case A. Obviously, the dotted line is approximate to the dashed line. Then, the estimated load torques tested by standard weights in case B (m_{load} = 0.5 kg) and case C (m_{load} = 1 kg) are shown in Figures 21c and 22c, where the estimated load torque (dotted line) is close to the theoretical results (dashed line). Eventually, the root mean square error is adopted to further evaluate the performance of the proposed torque observer in all three cases, of which all incidences with RMS errors are 0.17 Nm, 0.23 Nm, and 0.25 Nm.

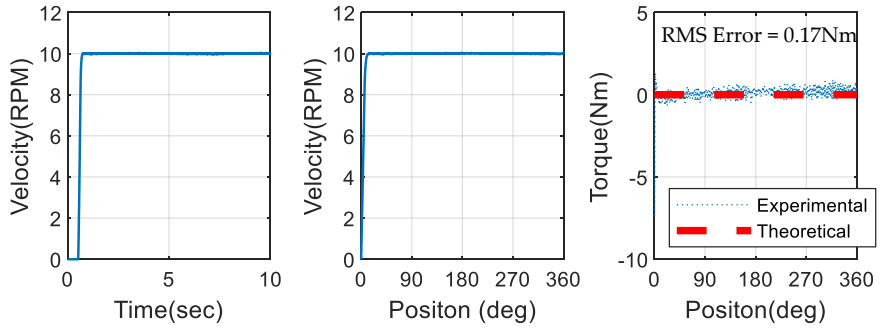

(**a**) Time vs. velocity (**b**) Position vs. velocity (**c**) Torque estimation

Figure 20. Validity of load torque estimation (case A: m_{load} = 0 kg).

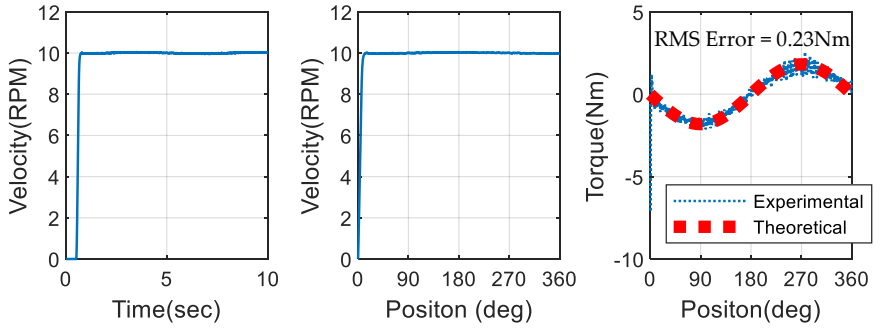

(**a**) Time vs. velocity (**b**) Position vs. velocity (**c**) Torque estimation

Figure 21. Validity of load torque estimation (case B: = 0.5 kg).

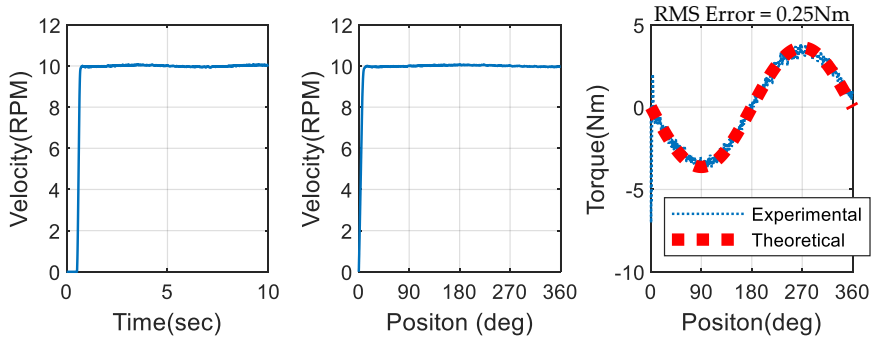

(**a**) Time vs. velocity (**b**) Position vs. velocity (**c**) Torque estimation

Figure 22. Validity of load torque estimation (case C: m_{load} = 1 kg).

4.3. Realize the Control of the Power-Assist System and Impedance Control

Based on the above examination of torque estimation, the torque sensorless power-assist system based on the observer can be verified with the configuration in Figure 23a, where the extra load attached at the end of the robot is 1 kg. Furthermore, the assistance power is realized by (14) with A_T = 0, 1, and 2. Since the experimental configuration is categorized in the power-assisted mode mentioned in Section 2, the results of the power-assisted ratio A_T = 0, 1, and 2 are depicted in Figure 24 with the operating range $\theta_{ROM} = 0 \sim 75°$ (0~1.31 rad). With $A_T = 0$ (without the assistance power) as shown in Figure 24a, the initial disturbance estimation is around –3.91 Nm, which occurs because of the extra load. To operate the one-link robot in the range of θ_{ROM}, the maximum human torque is 6.94 Nm. Then, the maximum human torque is reduced to 5.38 Nm due to the increased power-assisted ratio A_T = 1 as shown in Figure 24b. Eventually, the maximum human torque is decreased to 4.51 Nm at $A_T = 2$. Therefore, the human effort can be alleviated with the proposed torque sensorless power-assist system.

Further, the soft boundary based on the impedance control can be verified by the experimental setup in Figure 23b. The user pulls the handle attached to the end of the robot arm and the control system provides the impedance torque T_{imp} gently against the user's effort. Hence, the haptic effect of the soft boundary between the human and machine can be achieved. The parameters of the three cases for the impedance model are listed in Table 3, and the results of the impedance model are shown in Figure 25, where the dashed line indicates the variation of the robot arm position and the solid line presents the human torque $\hat{T}_h$.

Since stiffness κ is the extent to which an object resists deformation in response to an applied force, the definition of κ is expressed as $\kappa = force\ on\ the\ body\ (\hat{T}_h)/\ displacement$ in this study. In other words, the complementary perception is flexibility, compliance, or softness. The softer an object is, the less stiff it is. The result of case A is shown in Figure 25a; the human torque is smoothly increased according to the position information

and impedance parameters B_{imp} and K_{imp}, and the maximum $\hat{T}_h$ is around 19.2 Nm with the maximum position variation. Further, the stiffness κ gradually approaches 100 (Nm/rad). Then, K_{imp} in case B is two times that of case A, in other words, the stiffness in case B is slightly larger than in case A. Hence, the maximum $\hat{T}_h$ is about 23.2 Nm of the soft boundary in the maximum position variation in Figure 25b, and the stiffness κ gradually approaches 200 (Nm/rad). Finally, B_{imp} in case C is four times that of case A; to put it another way, it is difficult for the user to facilitate pulling the robot arm, and the result is presented in Figure 25c. Meanwhile, the stiffness κ is gradually approaching 100 (Nm/rad). To indicate the stiffness variation for presenting the characteristics of the soft boundary, the results are illustrated in Figure 26 during the position displacement close to the *ROM* limitation.

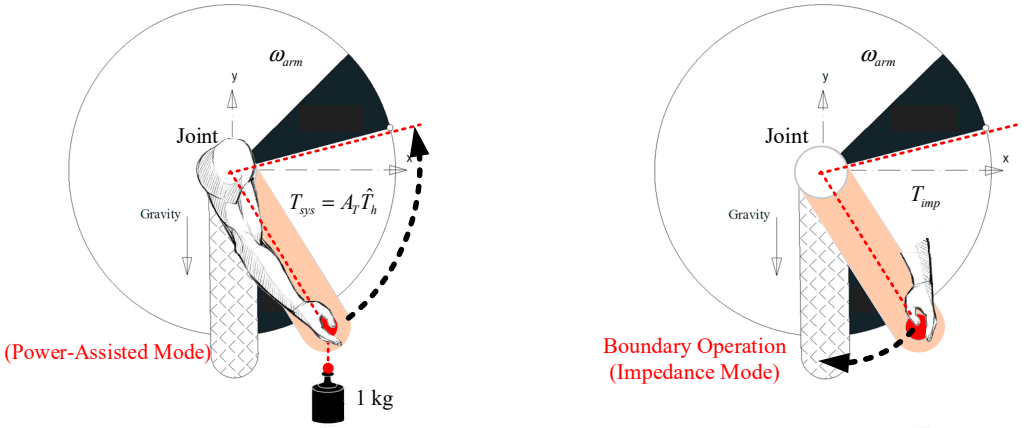

(**a**) Power-assisted mode (**b**) Impedance control mode

Figure 23. Experimental setup of power-assisted and impedance control mode.

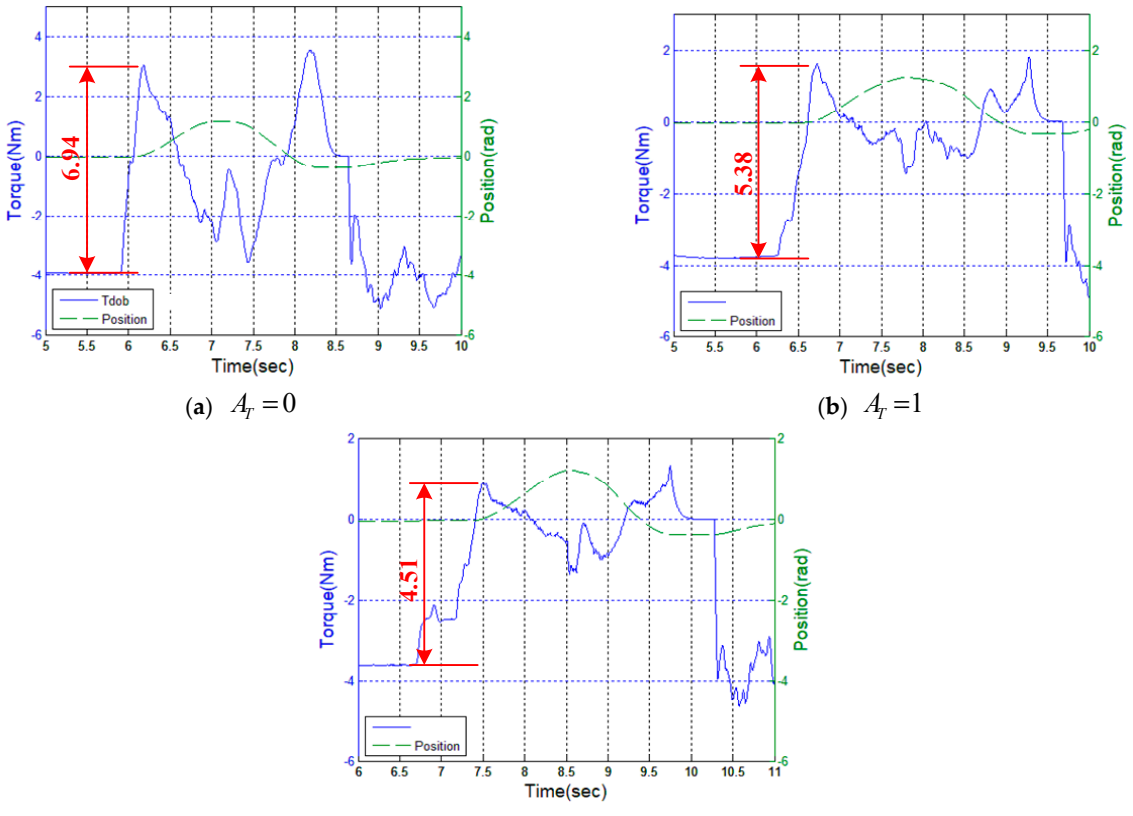

(**a**) $A_T = 0$ (**b**) $A_T = 1$

(**c**) $A_T = 2$

Figure 24. Responses of the power-assist mode with A_T = 0, 1, and 2.

Table 3. Parameters of the impedance mode.

Item	Parameters of the Impedance Model
Case A	$B_{imp} = 10\ (\mathrm{N \cdot m \cdot sec/rad})$, $K_{imp} = 100\ (\mathrm{N \cdot m/rad})$
Case B	$B_{imp} = 10\ (\mathrm{N \cdot m \cdot sec/rad})$, $K_{imp} = 200\ (\mathrm{N \cdot m/rad})$
Case C	$B_{imp} = 40\ (\mathrm{N \cdot m \cdot sec/rad})$, $K_{imp} = 100\ (\mathrm{N \cdot m/rad})$

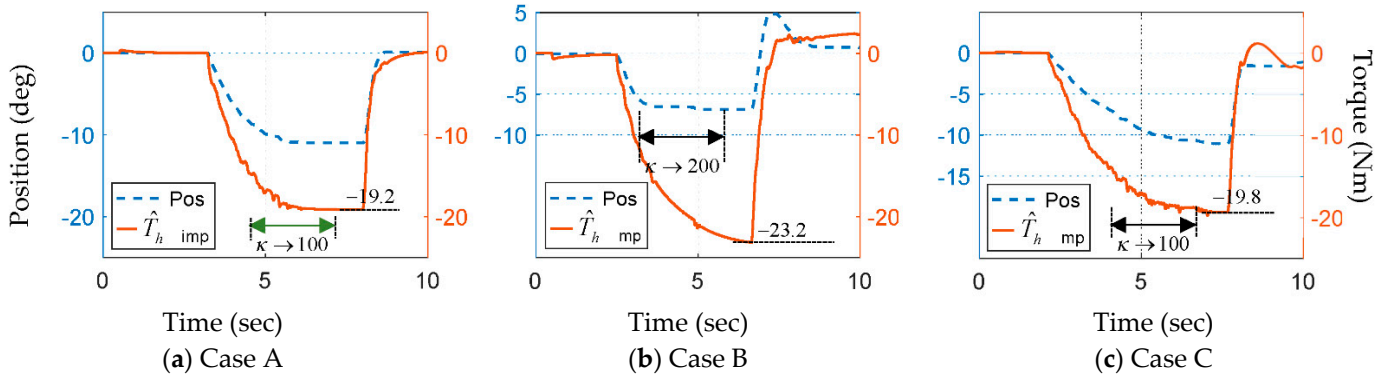

Figure 25. Result of the soft boundary realized by the impedance control.

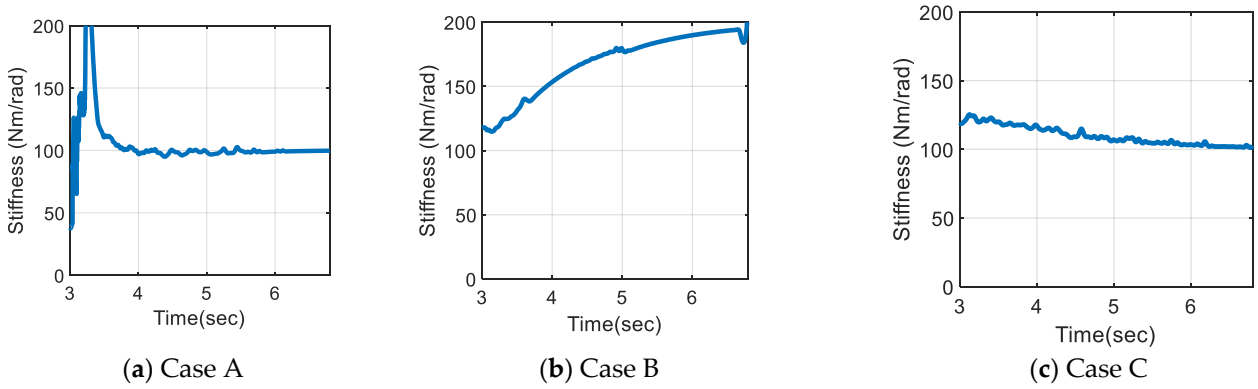

Figure 26. Stiffness variation of the soft boundary is realized by the impedance control.

5. Conclusion and Future Work

This paper proposes a model-based disturbance observer based on a PDFF type compensator to enhance the transient response of torque estimation. The transient response of PDFF 25 is better than that of the PDF typed compensator since the rising time is improved by about 26.4% from 0.072 s (PDF compensator) to 0.053 s (PDFF25 compensator). Then, the PDFF compensator was integrated into the model-based observer for estimating the external disturbance. The performance of torque estimation is verified in the experimental section. Evidently, the estimated load torque is approximately equal to the theoretical results, and the human effort is available to be alleviated with a proposed torque sensorless power-assist robot arm system based on torque estimation.

Further, due to the *ROM* limitation of the human joints, the risk of extreme flexing or extending in the power-assist robot arm system should be avoided. Thus, the virtual soft boundary was realized by the impedance control and integrated into the power-assist system. The compliance characteristic is comprehended in the boundary of the *ROM* according to the desired impedance model. Hence, the experimental results not only show the capability of the torque estimation and soft boundary but also ensure the stability of the power-assist robot arm system. Future work will focus on the experiment with a more powerful electric motor and heavy loads since the power-assist robot arm system may be operated for hard work in the future.

Author Contributions: P.-W.H. contributed to the research concept, methodology, data collection and data validation. W.-S.Y. provided the advice on the research. T.-M.K. contributed to the software development, experimental planning and execution, and data analysis. P.-W.H. wrote the manuscript draft. W.-S.Y. reviewed and revised the manuscript. All authors have read and agreed to the published version of the manuscript.

Funding: This research was funded by the Ministry of Science and Technology of Taiwan, under grant number MOST 110-2221-E-992-088.

Conflicts of Interest: The authors declare no conflict of interest.

References

1. Miller, J.S. *The Myotron—A Servo-Controlled Exoskeleton for the Measurement of Muscular Kinetics*; Final Technical Report of Cornell Aeronautical Lab Inc Buffalo: New York, NY, USA, 1968.
2. Garcia, E.; Jimenez, M.A.; de Santos, P.G.; Armada, M. The Evolution of Robotics Research—From Industrial Robotics to Field and Service Robotics. *IEEE Robot. Autom. Mag.* **2007**, *14*, 90–103. [CrossRef]
3. Kim, Y.; Yoon, W.C. Generating Task-Oriented Interactions of Service Robots. *IEEE Trans. Syst. Man Cybern. Syst.* **2014**, *44*, 9. [CrossRef]
4. Hao, M.; Cao, W.H.; Wu, M.; Liu, Z.T.; Li, S.H. An Initiative Service Method Based on Fuzzy Analytical Hierarchy Process and Context Interntion Inference for Drinking Service Robot. *IEEE Trans. Cogn. Dev. Syst.* **2019**, *11*, 221–233.
5. Tsai, M.C.; Hsueh, P.W. Force Sensorless Control of Power Assisted Wheelchair Based on Motion Coordinate Transformation. *Mechatronics* **2013**, *23*, 1014–1024. [CrossRef]
6. Hsueh, P.W.; Tsai, M.C. Reactive Torque Monitoring and Cycling Speed Control of a Belt-Driven Cycle Ergometer. *Control. Eng. Pract.* **2013**, *21*, 1564–1576. [CrossRef]
7. Hu, Y.; Benallegue, M.; Venture, G.; Yoshida, E. Interact with Me: An Exploratory Study on Interaction Factors for Active Physical Human-Robot Interaction. *IEEE Robot. Autom. Lett.* **2020**, *5*, 6764–6771. [CrossRef]
8. Hsueh, P.W.; Tsai, M.C.; Chen, C.-L. Stimulation Interval Evaluation for Lower-Limb Cycling Movement Based on Torque Observer. *Asia J. Control.* **2017**, *20*, 1–13. [CrossRef]
9. Wang, W.; Chen, J.; Ji, Y.; Jin, W.; Liu, J.; Zhang, J. Evaluation of Lower Leg Muscle Activities During Human Walking Assisted by an Ankle Exoskeleton. *IEEE Trans. Ind. Inform.* **2020**, *16*, 7168–7176. [CrossRef]
10. Ren, Y.; Wu, Y.N.; Yang, C.Y.; Xu, T.; Harvey, R.L.; Zhang, L.Q. Developing a Wearable Ankle Rehabilitation Robotic Device for in-Bed Acute Stroke Rehabilitation. *IEEE Trans. Neural Syst. Rehabil. Eng.* **2017**, *25*, 589–596. [CrossRef]
11. Oh, S.; Hata, N.; Hori, Y. Proposal of Human-Friendly Motion Control. In Proceedings of the 30th Annual Conference of the IEEE Industrial Electronics Society, Busan, Korea, 2–6 November 2004; pp. 436–441.
12. Tanako, N.; Iwama, T.; Kumagai, S.; Takanishi, A.; Lim, H. New Collistion Force Suppression Mechanism and Based Control of Human-Friendly Robot. In Proceedings of the 18th International Conference on Control, Automation and Systems, Pyeongchang, Korea, 17–18 October 2018.
13. Rocon, E.; Belda-Lois, J.M.; Ruiz, A.F.; Manto, M.; Moreno, J.C.; Pons, J.L. Design and Validation of a Rehabilitation Robotic Exoskeleton for Tremor Assessment and Suppression. *IEEE Trans. Neural Syst. Rehabil. Eng.* **2007**, *15*, 367–378. [CrossRef]
14. Zhu, J.; Wang, Q.; Huang, Y.; Wang, L. Adding Compliant Joints and Segmented Foot to Bio-Inspired Below-Knee Exoskeleton. In Proceedings of the IEEE International Conference on Robotics and Automation, Shanghai, China, 9–13 May 2011.
15. Shepherd, M.K.; Rouse, E.J. Design and Characterization of a Torque-Controllable Actuator for Knee Assistance During Sit-to-Stand. In Proceedings of the 38th Annual International Conference of the IEEE Engineering in Medicine and Biology Society, Orlando, FL, USA, 16–20 August 2016; pp. 2228–2231.
16. Hsueh, P.W.; Chen, J.C.; Yao, W.S.; Tsai, M.C.; Syu, W.C. Luenberger Observer-Based Impedance Control of Linear Servo Motor for a Desired Haptic System. In Proceedings of the International Automatic Control Conference, Nantou Country, Taiwan, 2–4 December 2013.
17. Pervez, A.; Ryu, J. Safe Physical Human Robot Interaction-Past, Present and Future. *J. Mech. Sci. Technol.* **2008**, *22*, 469–483. [CrossRef]
18. Liang, C.; Hsian, T. Admittance Control of Powered Exoskeletons Based on Joint Torque Estimation. *IEEE Access* **2020**, *8*, 94404–94414. [CrossRef]
19. Bao, X.; Sheng, Z.; Dicianno, B.E.; Sharma, N. A Tube-Based Model Predictive Control Method to Regulate a Knee Joint with Functional Electrical Stimulation and Electric Motor Assist. *IEEE Trans. Control. Syst. Technol.* **2020**, *29*, 2180–2191. [CrossRef]
20. Liu, H.; Huang, Q.; Tong, Z. Simulation and Analysis of a Full-Active Electro- Hydrostatic Powered Ankle Prosthesis. In Proceedings of the 19th International Conference on Advanced Robotics, Delo Horizonte, Brasil, 2–6 December 2019.
21. Johnson, C.T.; Lorenz, R.D. Experimental Identification of Friction and its Compensation in Precise, Position Controlled Mechanisms. *IEEE Trans. Ind. Appl.* **1992**, *28*, 1392–1398. [CrossRef]
22. Ellis, G. *Observers in Control System (A Practical Guide)*; Academic Press: Cambridge, MA, USA, 2002.
23. Ohm, D.Y. Analysis of PID and PDFF Compensators for Motion Control Systems. In Proceedings of the 1994 IEEE Industry Applications Society Annual Meeting, Denver, CO, USA, 2–6 October 1994.

24. Golnaraghi, F.; Kuo, B.C. *Automatic Control Systems 9/e*; John Wiley & Sons Inc.: Hoboken, NJ, USA, 2010.
25. Song, P.; Yu, Y.; Zhang, X. Impedance Control of Robots: An Overview. In Proceedings of the 2nd International Conference on Cybernetics, Robotics and Control, Chengdu, China, 21–23 July 2017.